# Integration of Heat Transfer, Stress, and Particle Trajectory Simulation

SBIR Phase I
Supported by DOE Office of Nuclear Physics

May 15, 2012

Topic 45b
Calabazas Creek Research Inc.
690 Port Drive
San Mateo, CA 94404

Thuc Bui, Principal Investigator
1074 Solana Drive
Mountain View, CA
650 948-5361
bui@calcreek.com

No proprietary information is included in this proposal

## Summary of the Phase I Program

Calabazas Creek Research, Inc. (CCR) proposed to implement heat transfer and stress analysis into CCR's 3D beam optics code Beam Optics Analyzer (BOA). For the Phase I program, CCR proposed to develop a heat transfer solver and verify performance. Implementation of stress analysis was planned for the Phase II program, if funding was approved. The tasks for the Phase I program were as follows:

1. Implement a 3D linear heat transfer solver with automatic and adaptive meshing
2. Examine and validate the new heat transfer solver accuracy and performance by comparison with known solutions and convergence
3. Improve the accuracy and smoothness of the power density fields at the terminal surfaces
4. Design GUI windows for heat transfer problems

Details for each task are provided later in this report. A summary for each task is presented below.

*Task 1. Implement a 3D linear heat transfer solver with automatic and adaptive meshing*

This task was successfully completed. A fully functional heat transfer solver was integrated with beam optics analysis. It uses a single CAD model for all analysis types. It is easy to use, simple to mesh, and accurate when using adaptivity. This solver is now included with the BOA distribution.

*Task 2. Examine and validate the new heat transfer solver accuracy and performance by comparison with known solutions and convergence*

Two analytical cases were simulated using the heat transfer solver. The model was compared with the analytical solution for both temperature profiles and heat transfer rates. Excellent agreement was demonstrated, confirming the solver's accuracy. The convergence rate matched the theoretical prediction.

*Task 3. Improve the accuracy and smoothness of the power density fields at the terminal surfaces*

This task was completed successfully with implementation of the global L2 projection. This provides the quadratic shape function for future upgrades of the field solver.

*Task 4. Design GUI windows for heat transfer problems*

The GUI screens were successfully designed in the Phase I program. In addition, the screens were actually built and integrated into the BOA product and are available for code users.

## Summary

The Phase I program completed all proposed tasks. In addition, the heat transfer solver was implemented into the BOA product, along with GUI screens and post processing capability. These features are now available to BOA users.

## Identification and Significance of the Problem or Opportunity, and Technical Approach

Calabazas Creek Research, Inc. (CCR) developed and currently markets Beam Optics Analyzer (BOA) in the United States and abroad. The project was funded by the U.S. Department of Energy SBIR program [1]. BOA is a 3D, charged particle optics code that solves the electric and magnetic fields with and without the presence of particles [2, 3, 4, 5]. It includes automatic and adaptive meshing to resolve spatial scales ranging from a few millimeters to meters. It is fully integrated with CAD packages, such as SolidWorks, allowing seamless geometry updates. With these capabilities, CCR includes iterative procedures for optimization [6, 7], including a fully functional, graphical user interface (GUI) [8, 9]. Recently, time dependent, particle in cell (PIC) capability was added, pushing particles synchronically under quasistatic electromagnetic fields to obtain particle bunching under RF conditions [12]. CCR added the heat transfer solver during this Phase I program [11].

A high power RF source often consists of a thermionic emitter, focus electrode, mod-anode, anode, and collector. The electrons dissipate their energy on some terminal planes, e.g. the collector walls in the form of heat, which can be quantified by a power density field. In existing state-of-the-art analysis tools, the particle simulator is required to output the power density field in a proprietary format as a boundary condition for another simulation package for heat transfer analysis. This requires the designer to re-import the CAD drawings into the heat transfer package, re-specify the boundary conditions and material properties, and re-mesh before performing the analysis to obtain the temperature and stress information. This is time consuming and prone to many errors due to importing geometry and solution fields from one analysis tool to another. It is also expensive to purchase and maintain two different sets of analytical tools and the auxiliary codes interfacing the two.

In the Phase I program, Calabazas Creek Research. Inc. investigated the integration of heat transfer analysis with particle simulation in a single package. The package uses the same geometry imported from CAD, requiring input of material properties and boundary conditions only once. Mesh generation was automatic for all solvers, including the electromagnetic and thermal solvers.

The Phase I effort focused on developing higher orders of interpolation of the power density field and implementation of the heat transfer solver in BOA. Particular emphasis focused on integration of the initial meshes, since the particle simulator is more interested in the vacuum region, while the heat conduction analysis only concerns solid regions. BOA uses the same CAD model for both analyses, so it must generate two different meshes: one with and one without the vacuum region. CCR was able to achieve all proposed goals of the program and more. The technical achievements in Phase I are described in the sections that follow.

## Results of the Phase I Program

The main goal of the Phase I program was to implement a higher order power density field and 3D linear heat transfer field solver. The program not only provided an accurate and robust heat transfer solver but also integrated it into BOA. Specifically the Phase I objectives were:

- Implement a 3D finite element heat transfer solver with adaptivity
- Determine the accuracy of the linear heat transfer field solver to provide the basis for development of higher order solvers in Phase II
- Provide more accurate and smoother power density fields
- Define the geometry using the same CAD model, while maintaining different meshes, and interfacing the power density field between the particle simulator and heat transfer solvers

These objectives were achieved using modern programming techniques and algorithms. All programming was in C++ and parallelization in OpenMP, utilizing state-of-the-art multi-core technology. Both x86 and x64 versions are supported. The GUI design and implementation used Microsoft Foundation Class (MFC).

There were four specific tasks proposed for the Phase I program:

- Implement a 3D linear heat transfer solver with automatic and adaptive meshing
- Examine and validate the new heat transfer solver accuracy and performance using comparison with known solutions, including order of convergence verification
- Improve the accuracy and smoothness of the power density fields at the terminal surface
- Design GUI windows for specifying boundary conditions, material properties, and post-processing.

The technical achievements of each task are described below.

### *Task 1. Implement a 3D linear heat transfer solver with automatic and adaptive meshing*

The Phase I program successfully integrated a steady state, 3D, linear heat transfer, finite element solver into Beam Optics Analyzer with auto meshing and adaptivity. The new solver is fully integrated with beam optics analysis, allowing seamless switching between analysis types. It is also fully parallelized with OpenMP.

Before describing the solver implementation and performance, integration issues are discussed. The main goal of the program is to create an intuitive, user friendly, design tool, requiring as little user input as possible to simulate the initial design. This is achieved by using the same solid model for all analysis types, including beam optics, heat transfer, and stress analysis. Unfortunately, the domain for the particle simulator is the vacuum region, while the domain for the heat transfer simulation is the solid regions. Thus, the heat transfer mesher and solver must isolate the vacuum region and model only the solid regions. For example, BOA imports a single solid model from SolidWorks, shown in Figure 1. This electron gun includes a focus electrode, mod anode and capped anode. The anode cap is included to capture the beam for the later heat transfer analysis.

BOA uses the same solid CAD model for all analysis types. For magnetostatics , electrostatics and beam optics analysis, it creates a background region enclosing the model. As an option, the user can suppress the background region and select symmetry to reduce computational resources, as shown in the GUI window. In this case BOA creates a separate companion model including the background region and required symmetry for each analysis type, although electrostatics and

beam optics use the same companion model. The original model is untouched; however, if it is modified by the Optimizer or the user, BOA automatically updates the companion models and the prescribed boundary conditions. The mesher in BOA generates different meshes appropriate for each analysis type. The left side of Figure 2 shows the initial mesh for the beam optics analysis with the background enclosure, and the right side shows the heat transfer mesh, where only the solids are considered. The beam optics mesh comprises 289,152 tetrahedra, 578,700 faces and 49,348 vertices; however, the heat transfer comprises only 11,704 tetrahedra, 24,995 faces and 2,864 vertices. Maintaining internally separate meshes dramatically reduces the computer resource requirements when integrating heat transfer with beam optics.

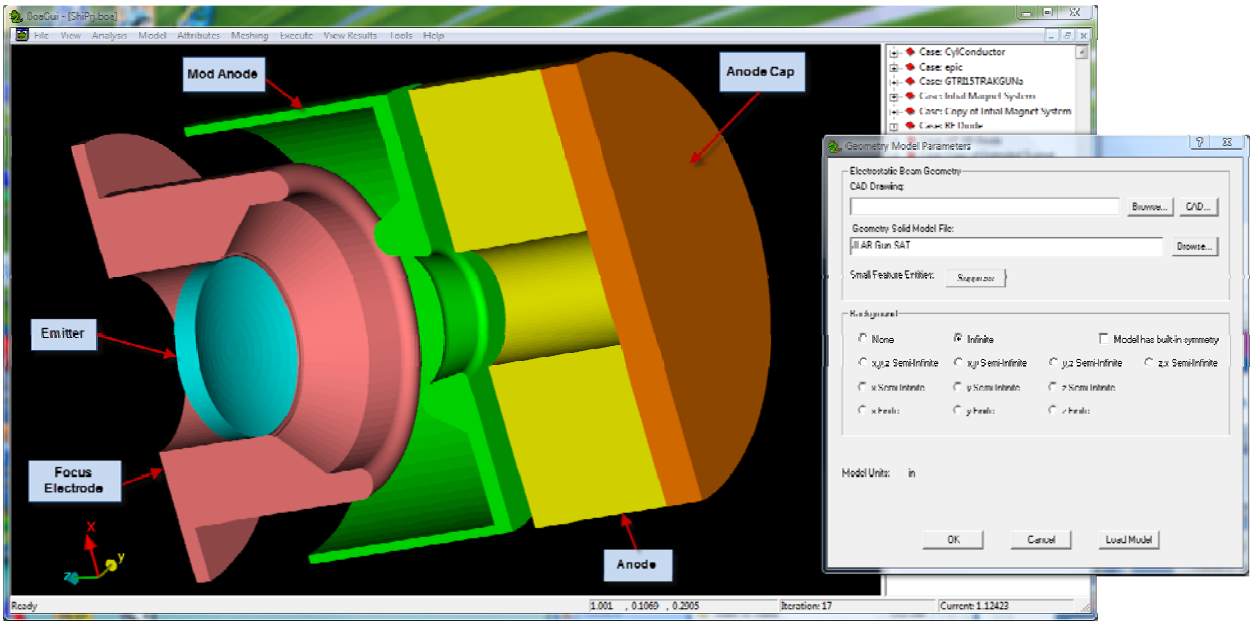


**Figure 1** A mod anode electron gun imported from SolidWorks

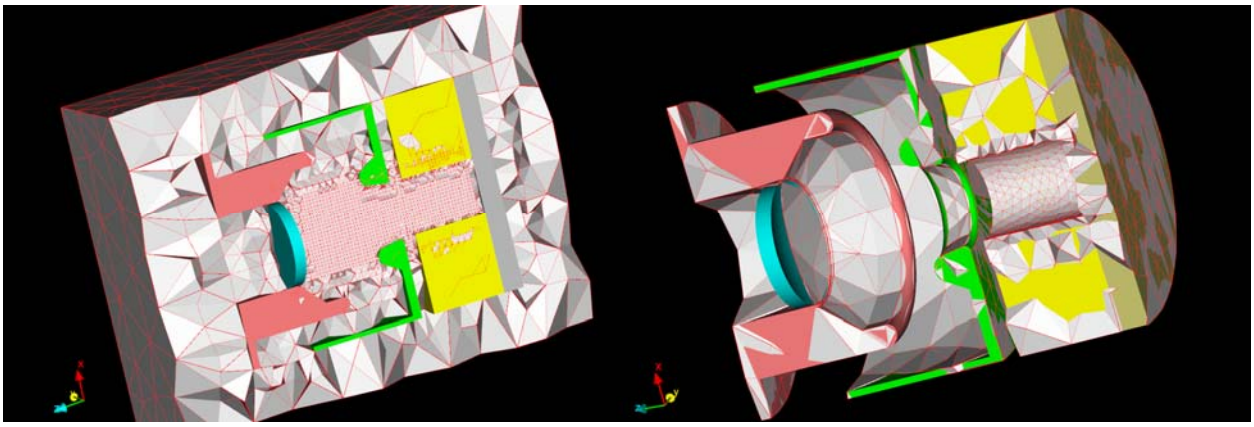

**Figure 2** Initial mesh **(a)** for beam optics **(b)** for heat transfer

Computational resources can be reduced further by making non-critical components invisible to the mesher without modifying the original CAD model, as shown in Figure 3. Here the emitter, focus electrode, and mod anode are removed from the heat transfer analysis. This feature will be implemented in Phase II.

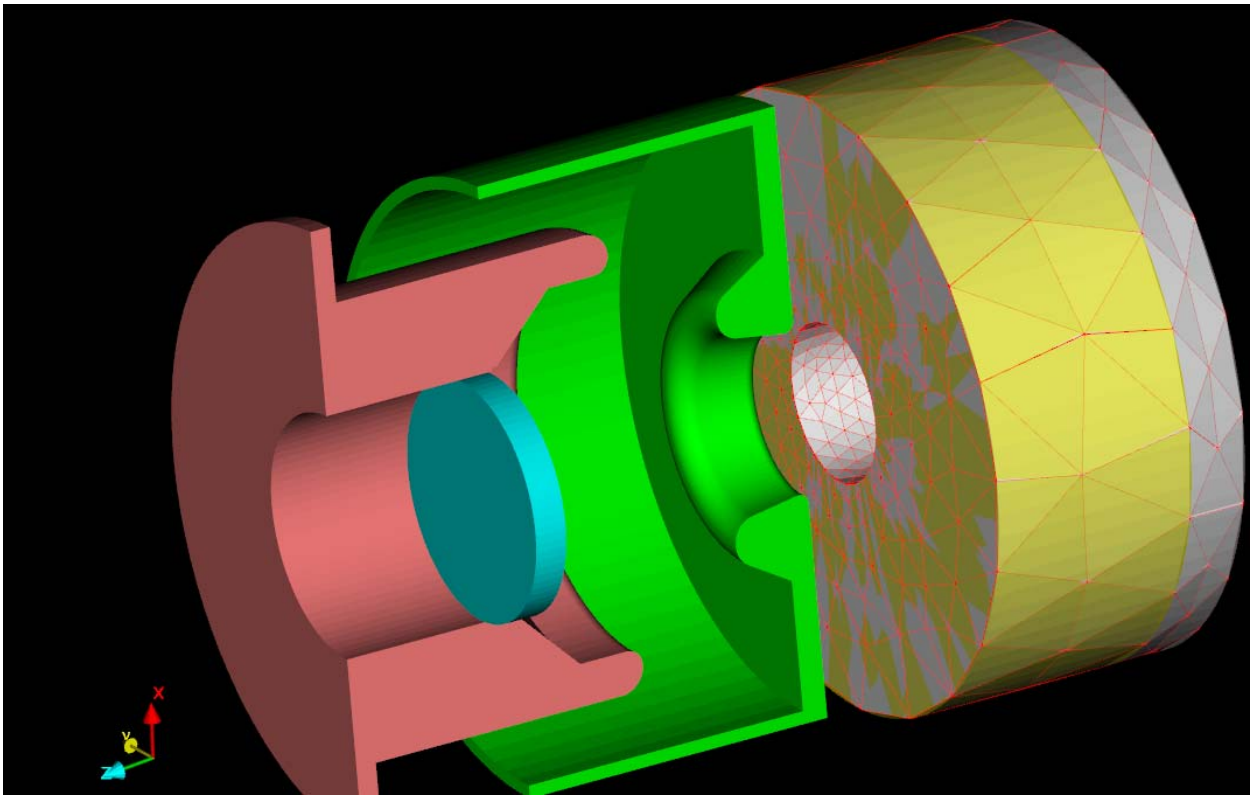


**Figure 3** Future implementation mesher where only critical parts specifiable by users to be included in simulation

Starting with a mesh, such as in Figure 2b, the heat transfer analysis solves the steady state heat equation

$$\nabla \mathbf{q} = f \tag{1}$$

where $f$ is the heat input per unit volume, and $\mathbf{q}$ is the heat flux vector defined in terms of temperature gradient by the generalized Fourier law:

$$\mathbf{q} = -\kappa \nabla T \tag{2}$$

where the conductivities $\kappa$ are given functions of $\mathbf{x}$. This conductivity matrix is assumed positive definite. The heat transfer currently assumes the most common, isotropic materials in which the thermal conductivity is single valued for all three spatial directions. Anisotropic materials will be added in the Phase II program. To close the problem, the heat equation must also satisfy the prescribed Dirichlet and Neumann boundary conditions

$$T = T_0 \qquad \text{on } \Gamma_d \tag{3}$$

$$-\mathbf{q} \cdot \mathbf{n} = q_{s0} \qquad \text{on } \Gamma_n \tag{4}$$

Across region interfaces of different materials, the following continuity condition for the normal component of the heat flux vector without the surface heat density must also be met:

$$\left(\mathbf{q}_1 - \mathbf{q}_2\right)\cdot\mathbf{n} = 0 \tag{5}$$

Instead of working with the strong form above, the finite element approach in BOA works with its variational or weak form. One can discretize the problem domain as $\Omega = \bigcup_{e=0}^{n_{el}} \Omega^e$ where $\Omega^e$ is the element domain to obtain the integral, weak formulation from the strong form

$$\sum_{e=1}^{n_{el}} \int_{\Omega^e} \nabla W \cdot \kappa \nabla T \; d\Omega = \sum_{e=1}^{n_{el}} \int_{\Omega^e} Wf \; d\Omega + \int_{\Gamma_n^e} W q_{s0} \; d\Gamma \tag{6}$$

Solving for $T$ in Eq. (6) requires more specialization of the trial solutions and weighting functions, particularly in the element domains. A typical member of the weighting functions in each element is assumed to have the form

$$W\left(\mathbf{x}\right) = \sum_{a=1}^{n_{en}} N_a\left(\mathbf{x}\right) \; w_a \tag{7}$$

where $N_a$ is the interpolation or shape function associated with element node number $a$, $w_a$ is a constant, and $n_{en}$ is the number of element nodes. These are required to be linearly independent throughout. Likewise, for trial solutions

$$T\left(\mathbf{x}\right) = \sum_{a=1}^{n_{en}} N_a\left(\mathbf{x}\right) T_a \tag{8}$$

where $T_a$ is the unknown temperature at element node $a$ and

$$T_0\left(\mathbf{x}\right) = \sum_{a=1}^{n_{en}} N_a\left(\mathbf{x}\right) T_{0a} \tag{9}$$

Similarly,

$$f\left(\mathbf{x}\right) = \sum_{a=1}^{n_{en}} N_a\left(\mathbf{x}\right) f_a \tag{10}$$

$$q_{s0}\left(\mathbf{x}\right) = \sum_{a=1}^{n_{en}} N_a\left(\mathbf{x}\right) q_{sa} \tag{11}$$

Substituting Eqs. (7) to (11) into Eq. (6) yields

$$\sum_{e=1}^{n_{el}} \left( \int_{\Omega^e} \nabla N_a \cdot \kappa \nabla N_b \; d\Omega \right) T_b = \sum_{e=1}^{n_{el}} \left( \int_{\Omega^e} N_a N_c f_c \; d\Omega + \int_{\Gamma_n^e} N_a N_c q_{sc} \; d\Gamma \right) \tag{12}$$

where repeated indices indicate implicit sums and $1 \le a,b,c \le n_{en}$. Equation (12) is the finite element matrix formulation to solve for the nodal temperature $T_b$. The integral on the left hand side is often called the Dirichlet matrix. It is symmetric and positive-definite.

Shape functions must be selected in such a way that, as the finite element mesh is refined, the approximate variational solution converges to the exact solution. Sufficient conditions on the shape functions for convergence are that they be (1) smooth on each element interior, (2) continuous across each element boundary, and (3) complete. These convergence conditions guarantee that first derivatives of the shape functions have, at worst, finite jumps across the element interfaces. This ensures that all integrals necessary for the computation of element arrays in Eq. (12) are well defined, since, at most, first derivatives appear in the integrals. They also require a shape function capable of exactly representing an arbitrary linear polynomial when nodal degrees of freedom are assigned to the element nodes. This will ensure that the constant values over each element domain are representable as the exact solution and its first derivatives are recalculated as the finite element mesh is further and further refined. Lagrange polynomials are used for the shape functions in both electrostatics and heat transfer solvers. They could be of any order, but due to time constraints, only linear tetrahedral elements were implemented for the heat transfer solver in the Phase I program. Quadratic tetrahedral elements will be implemented in the Phase II program to improve the field fidelity for a given mesh.

Isoparametric elements were implemented in the heat transfer solver. With isoparametric elements, both spatial and field element interpolations are the same, and the three above basic convergence conditions are virtually automatic. In addition, the standard finite element formulation intrinsically ensures continuity, although this is weakly (by integration instead of pointwise) ensured for normal components of the heat flux vector across the element interfaces. For the piecewise linear finite element space, the discrete temperature is linear, and the discrete temperature gradient is uniform on the element interior.

A procedure was also implemented to smooth out the computed gradient to produce a $C^0$-continuity finite element space. This important procedure provides the accuracy and smoothness of temperature gradients when calculating error estimates required for adaptive meshing. The finite element method produces the optimal approximation from the finite element spaces. However, it is frequently the case that one is more interested in the gradient of the finite element approximation than in the approximation itself. As mentioned above, the discrete temperature gradient vector is discontinuous across the element boundaries, meaning that the approximation of the main quantity of interest is discontinuous. For this reason, the heat transfer solver implemented a post-processing procedure, whereby the discontinuous approximation to the gradient of the temperature was smoothed. It is important to note that even though the temperature gradient is discontinuous across the element interfaces in the finite element formulation, the normal component of heat flux is weakly, in the integral sense, continuous. The reasons to perform such post-processing to smooth out the gradient field are not purely cosmetic. The main reason for post-processing of the gradient field is to estimate *a posteriori* the error for mesh adaptivity. A rather natural approach to the error estimation is based on measuring the difference between the direct and post-processed (recovered) approximation to the gradient. The approach uses the procedure developed by Zienkiewicz and Zhu [14, 15, 16, 17]. Their so-called superconvergent patch recovery (*SPR*) procedure post-processes the finite element approximation to obtain values of the gradient field at the nodes. These are the *recovered*, averaged, and smoothed gradients sampled from the centroids of all elements sharing a common node. These values are then used to obtain the globally reconstructed gradient field, producing a

$C^0$-continuous gradient field. The recovered gradient is then compared with the unprocessed field gradient to obtain the posteriori error estimate.

In more detail, the *SPR* procedure creates at each vertex of the mesh a patch consisting of the elements having the same vertex. The values of the gradients of the approximation sampled at the centroids (for linear tetrahedral elements) in the patch produce a recovered value at the central node by a discrete least squares fit of the values at the sampling points. The reason for sampling the gradient at the centroids of linear tetrahedral elements is because of the well known fact that the gradient at a centroid is *superconvergent* [18]. Superconvergence means that the gradient evaluated at a centroid is as good as the true value in terms of a seminorm. Thus, the *SPR* method creates a local patch field at each mesh vertex to form a globally smoother field.

Beam optics analysis of the electron gun model of Figure 1, with the mesh of Figure 2a, produces a beam that generates a power density field on the anode cap, shown in Figure 4. The surface power density field with its mesh is shown in Figure 4b, as a close-up. This beam optics analysis required 354.5s of CPU time in an 8-core PC.

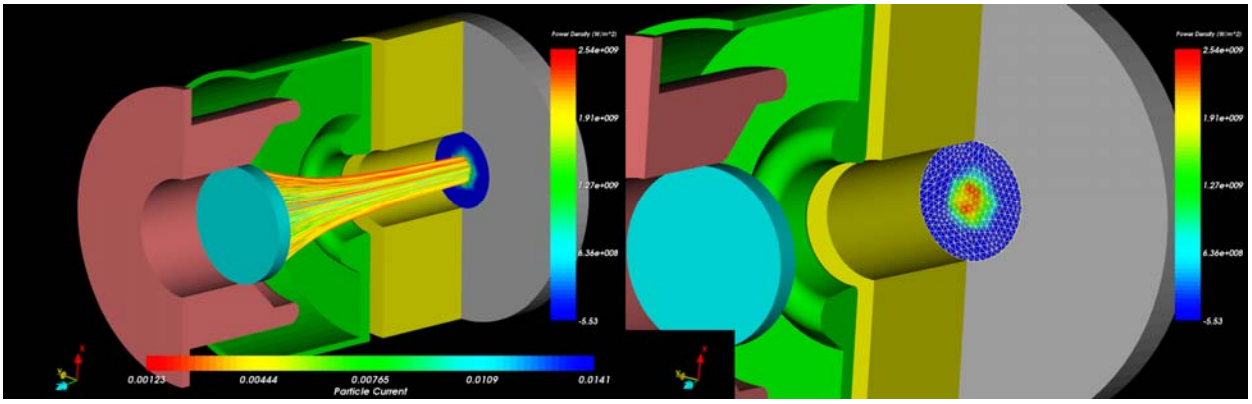


**Figure 4 (a)** Electron beam and its generated power density **(b)** A close-up of the power density field with its mesh

To use this power density field in a heat transfer analysis, the user invokes the GUI to change the analysis type. The analysis uses the power density field as the heat flux on the anode cap and applies boundary conditions, such as prescribed temperatures or convection cooling. For this example, convection cooling is specified on the anode outer diameter and cap. In addition, the power density field is scaled for 5% duty, to avoid temperatures above the copper melting point. This ability to scale the power density field is included in the heat transfer GUI. The temperature profile generated from this power density without adaptivity is displayed in Figure 5. The left side shows the temperature contour on the anode cap, and the right side shows the temperature profile in color gradient fill with the initial mesh.

Invoking adaptive meshing provides more accurate results and a smoother temperature profile, as shown in Figure 6. Without adaptive meshing, the analysis underestimates the temperature more than 100°C. The extra computational cost of adaptivity for heat transfer analysis is minimal and requires no extra effort from the user. The CPU time required without adaptivity was 2.38s, while the time required with adaptivity was 7.92s in an 8-core PC. The adaptive mesh solution required 12,706 tetrahedra and 2,705 vertices.

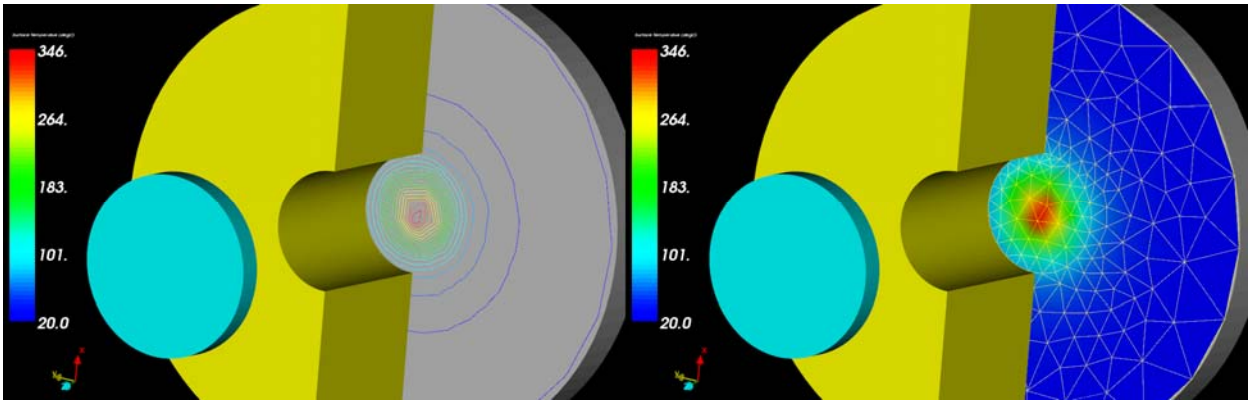


**Figure 5** Temperature **(a)** as contour on the anode cap **(b)** as color gradient fill with the initial, non-adaptive mesh

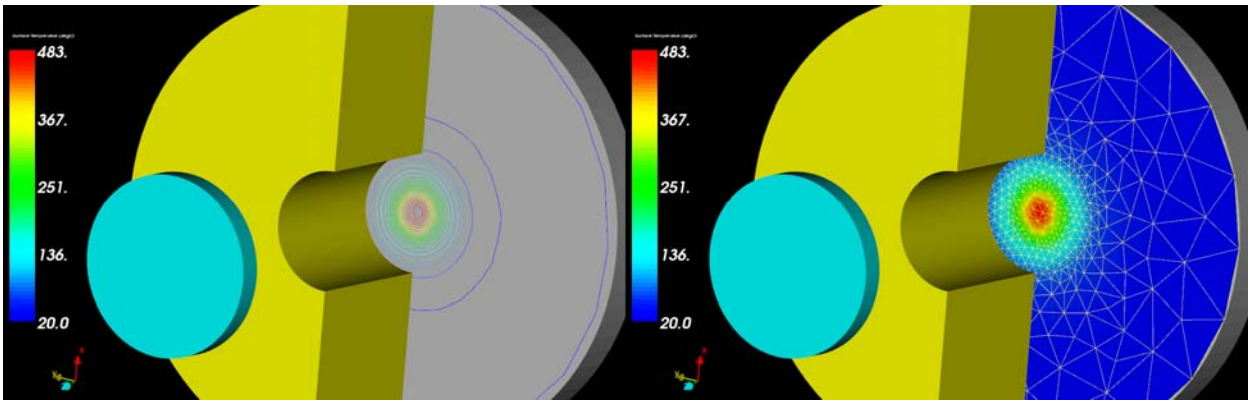


**Figure 6** Temperature **(a)** as contour on anode cap (b) as color gradient fill with adaptive mesh

The next example demonstrates use of BOA to design a collector for a multiple beam klystron, as shown in Figure 7. Fifteen spent beams are injected into a collector, which is cooled by convection. These fifteen spent beams generated a power density field on the collector inner surface. The beam optics analysis required an hour of CPU time to complete, and the results are shown in Figure 8. This power density field is used as a heat flux boundary condition in the heat transfer analysis. Figure 9 compares the initial mesh with the adapted mesh, which comprised 865,231 tetrahedra and 172,393 vertices. Figure 10 shows the temperature profile using the adaptive mesh. The heat transfer analysis with adaptivity requires 308s.

This task demonstrated a fully functional heat transfer solver integrated with beam optics analysis. It uses a single CAD model for all analysis types. It is easy to use, simple to mesh, and accurate when using adaptivity.

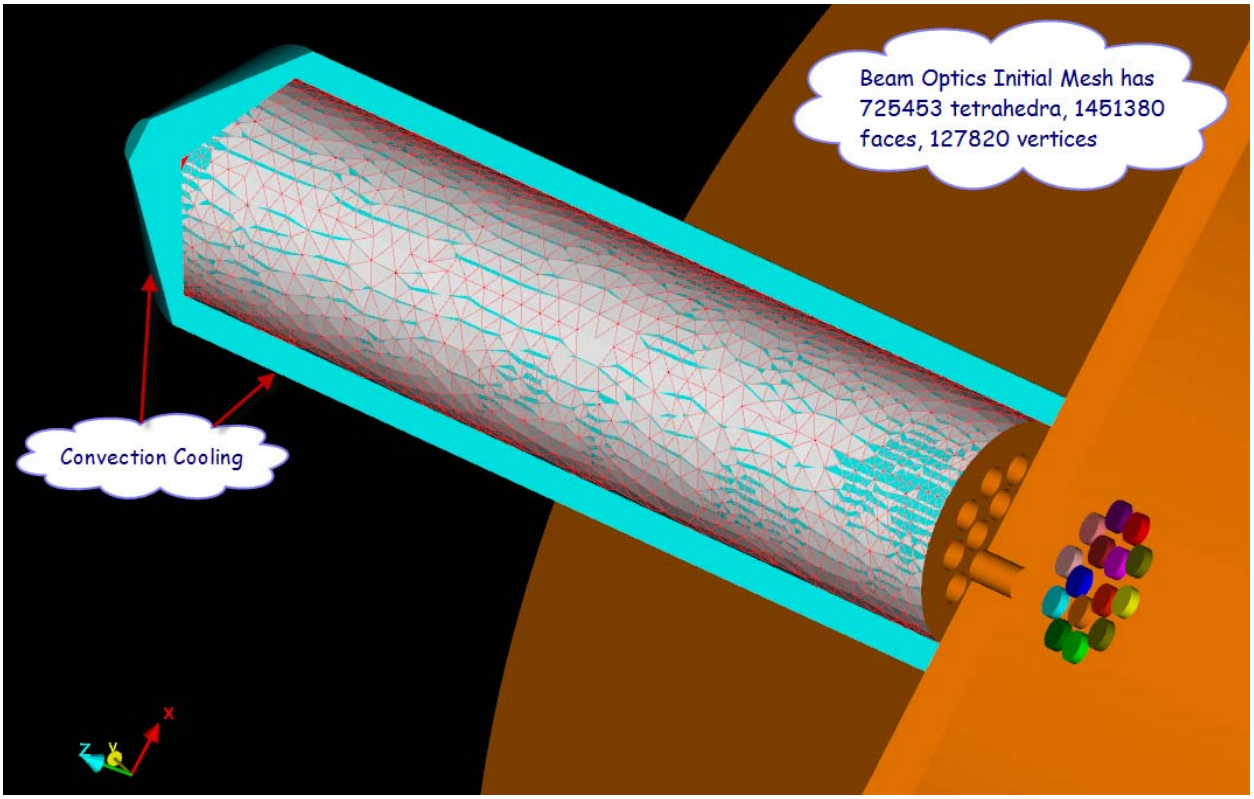


**Figure 7** A collector for 15 electron beam. Also shown are the initial surface meshes on the collector ID.

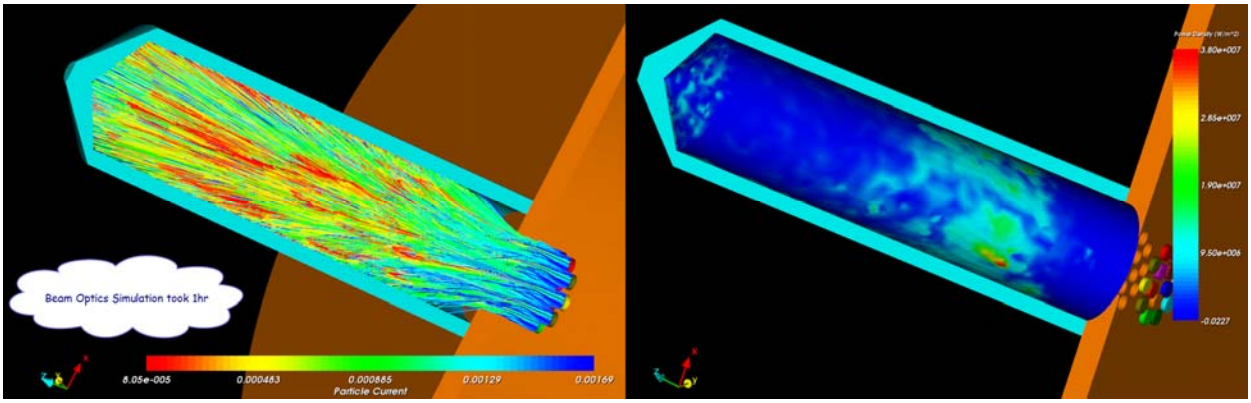


**Figure 8** A collector for 15 electron beam **(a)** Particle trajectories **(b)** Beam generated power density

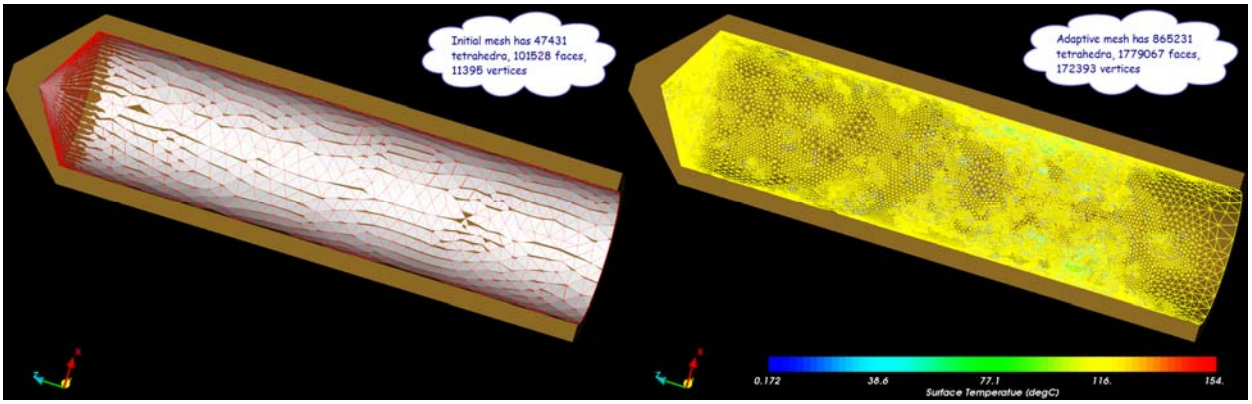


**Figure 9 (a)** Initial meshes **(b)** Adaptive meshes on the collector ID

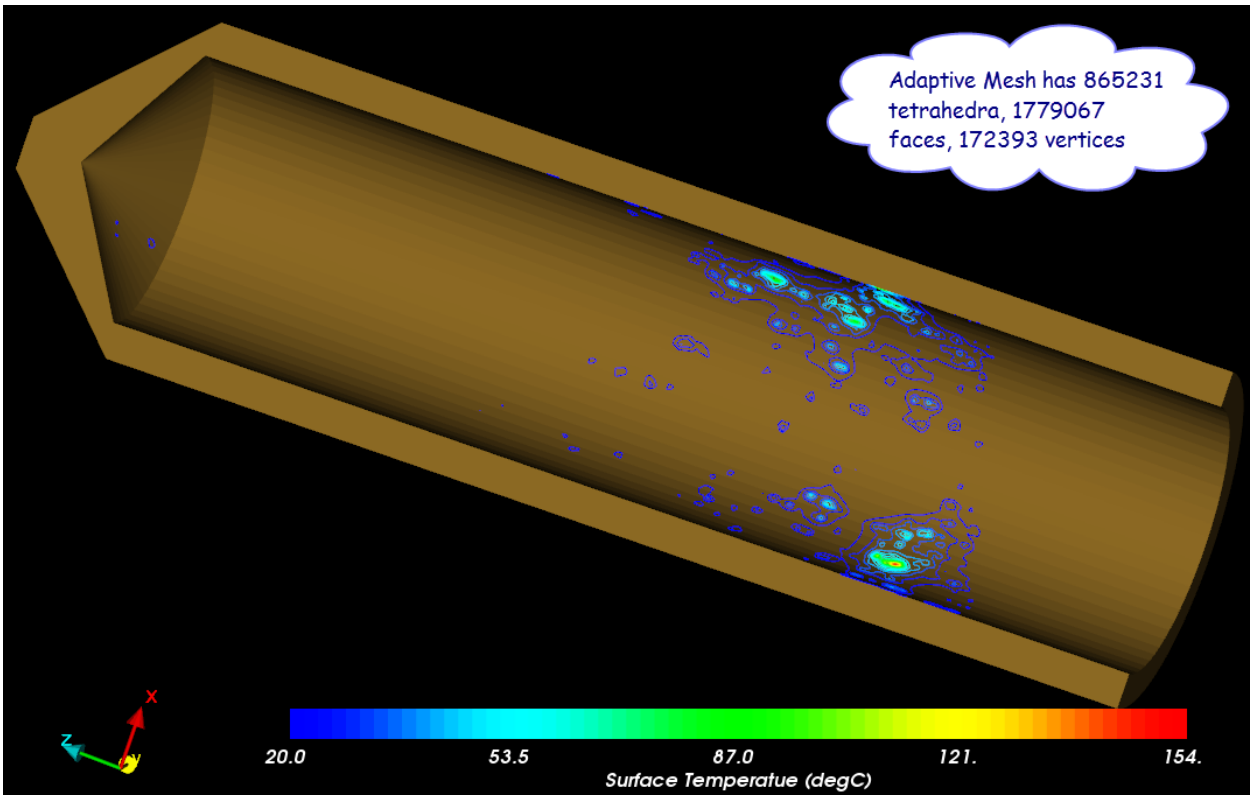


**Figure 10** Adaptivity temperature as contour on the collector OD

### *Task 2. Examine and validate the new heat transfer solver accuracy and performance by comparison with known solutions and convergence*

Validations used two test problems involving a cube with a uniform heat source. In one case, both end faces were prescribed temperatures (Dirichlet). In the other case, one end was assigned a heat flux (Neumann) and the other with a temperature. There are analytical solutions to such problems.

A unit cube with a uniform heat source $\dot{q}$ and each end, in the $x$ direction, prescribed with the temperature $T_o$ and $T_1$ respectively has the analytical solution

$$T = -\frac{\dot{q}}{2k}x(x-1) + (T_0 - T_1)x + T_i \tag{13}$$

where $k$ is the material thermal conductivity. Substituting $\dot{q} = 1\times10^6\ {}^{W}\!/_{m^3}$ and $T_0 = T_1 = 0$ with $k = 393.5\ {}^{W}\!/_{m\cdot{}^oC}$ into Eq. (13) yields

$$T = 1270.7x(1-x) \tag{14}$$

This exact solution is plotted against the finite element (FE) solution in Figure 11, showing they are very well matched even though the mesh for this FE solution used only 4,029 tetrahedra and 982 vertices. The raw and smoothed finite element temperature gradients versus the exact solution are plotted in Figure 12. The raw finite element temperature gradient solution in a linear element is, as expected, uniform and pointwise discontinuous across their interfaces. However, the heat flux intrinsically included in the finite element method is weakly continuous across the element interfaces in the integral sense. The smoothed temperature gradient produced by the *SPR* scheme precisely matches the exact solution, except at the boundaries. Better match at the boundaries is expected when the mesh is refined.

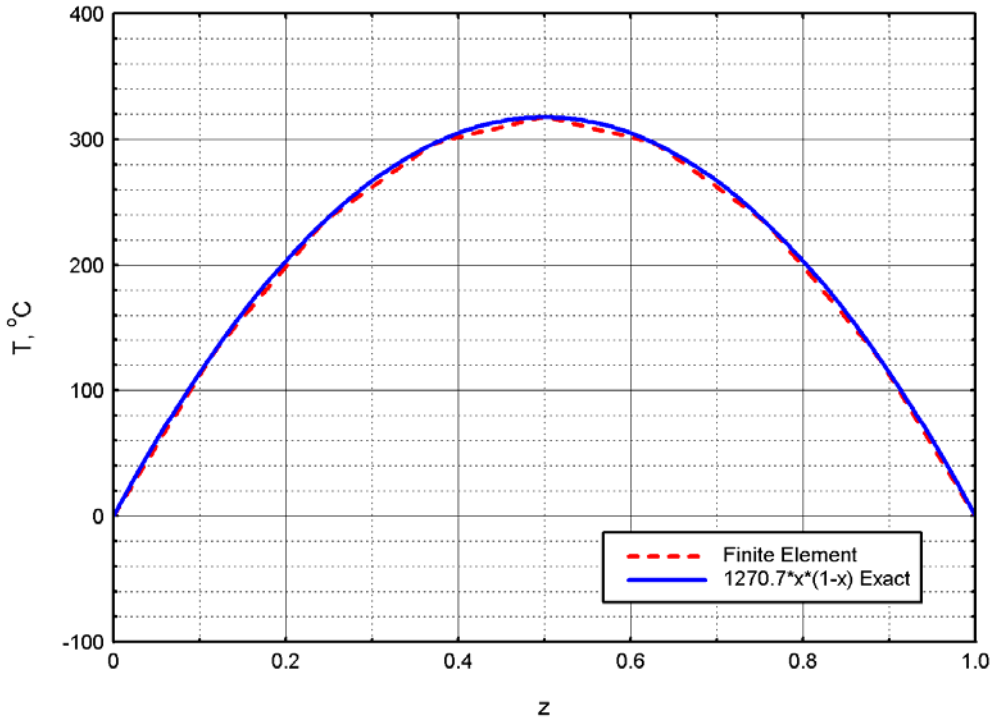


**Figure 11** FE versus exact temperature in a unit cube having a uniform heat source and homogeneous BC

The unit cube with a uniform heat source $\dot{q}$ and one end prescribed with a heat flux $q_0''$ and the other end zero temperature has the exact solution

$$T = \frac{\dot{q}}{2k}(1-x^2) + \frac{q_0''}{k}(1-x) \tag{15}$$

Substituting again $\dot{q} = 1\times10^{6}\ {}^{W}\!/_{m^3}$, $k = 393.5\ {}^{W}\!/_{m\cdot{}^{o}C}$ and $q_0'' = 1\times10^{4}\ {}^{W}\!/_{m^2}$ into Eq. (15) yields

$$T = (1-x)\left[1270.7(1+x)+25.414\right] \tag{16}$$

This exact solution is compared with the finite element solution in Figure 13, showing excellent agreement. The raw and smoothed temperature gradients are compared with the exact gradient in Figure 14. The raw FE gradient is, as expected, uniform in each element and discontinuous pointwise across the element interfaces. The smoothed FE field is in excellent agreement with the exact solution, except at the boundaries. Better match is also expected as the mesh is refined.

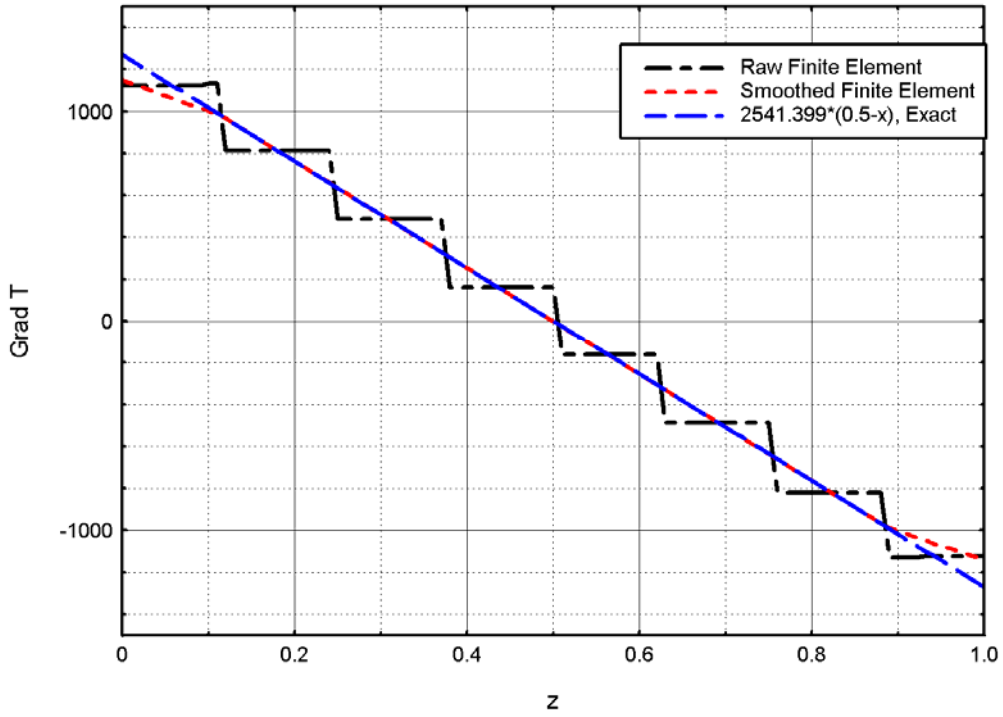


**Figure 12** FE raw and smoothed temperature gradient versus exact solution in a unit cube with a uniform heat source and homogeneous boundary condition at both ends

This task next compared the numerical rate of convergence with the theoretical rate. Szabo and Babuska [13] provide an error estimate as a function of the number of degrees of freedom when the exact solution is smooth, i.e., no singular points inside the solution domain or on its boundary, as follows

$$\|e\|_1 \le \frac{c}{N^k} \tag{17}$$

where $c$ is a positive constant, $k$ the polynomial degree of elements, $N$ the number of degrees of freedom, $T^h$ the finite element solution, $T$ the exact solution and

$$\|e\|_1 = \left[\int_\Omega \nabla^2 \left(T^h - T\right)\, d\Omega\right]^{1/2} \tag{18}$$

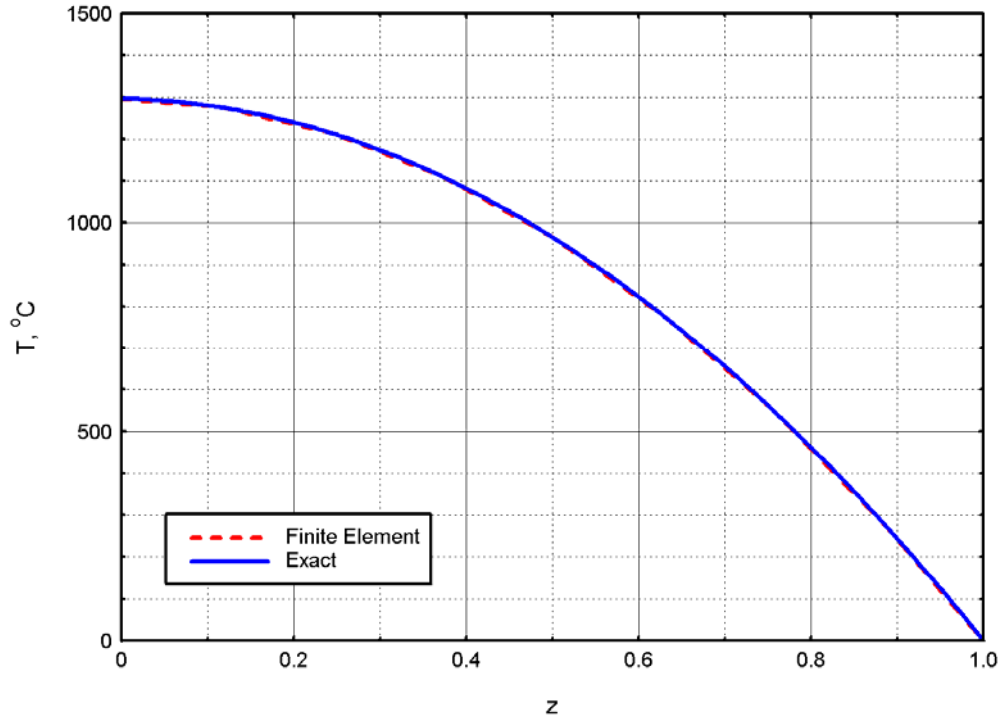


**Figure 13** Finite element temperature versus exact solution in a unit cube with a uniform heat source, heat flux at the left end and zero temperature at the right end

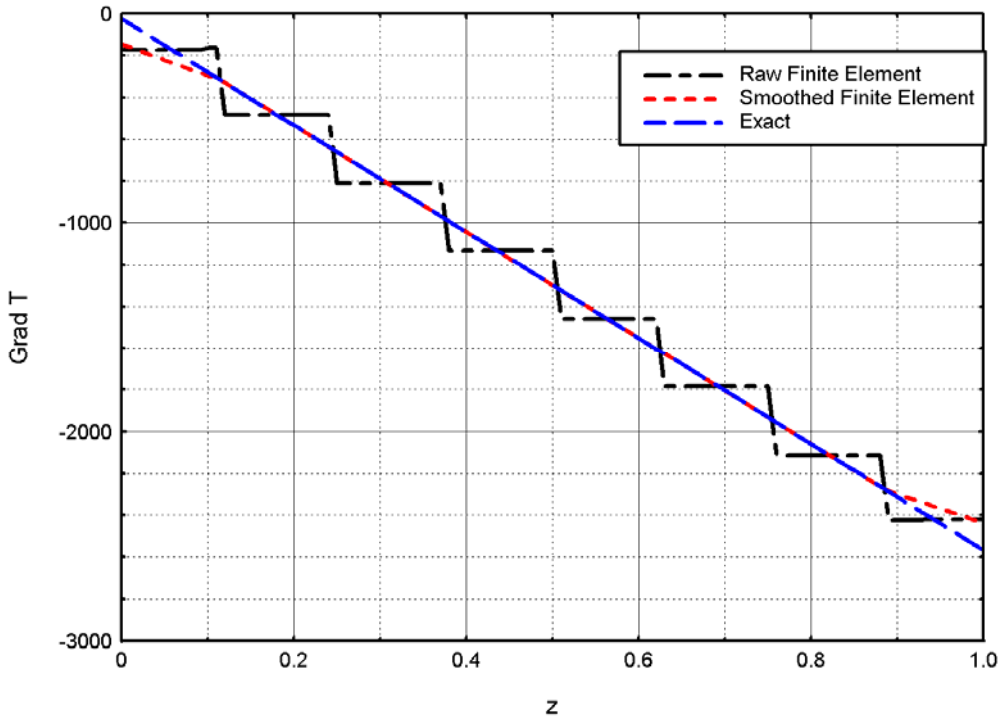


**Figure 14** FE raw and smoothed temperature gradient versus exact solution in a unit cube with a uniform heat source, heat flux at the left end and zero temperature at the right end

Equation (18) can also be simplified to [10]

$$\|e\|_1 = \left| \int_\Omega \nabla T \cdot \nabla T \, d\Omega - \int_\Omega \nabla T^h \cdot \nabla T^h d\Omega \right|^{1/2} \tag{19}$$

Substituting Eq. (19) into Eq. (17) yields the error energy norm estimate

$$\|e\|_1 = \left| \int_\Omega \nabla T \cdot \nabla T \, d\Omega - \int_\Omega \nabla T^h \cdot \nabla T^h d\Omega \right|^{1/2} \le \frac{c}{N^k} \tag{20}$$

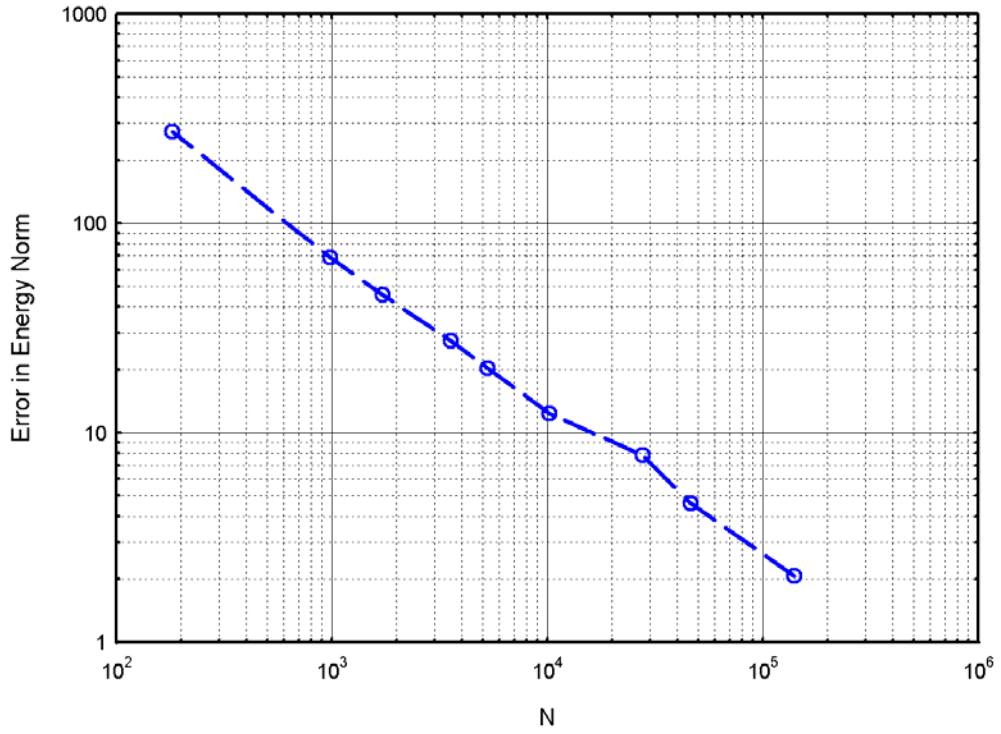


**Figure 15** Convergence rates for nonuniform mesh refinement, interpolation order is $k = 1$

The first integral is the energy norm of the exact solution, and the second integral is the finite element energy norm. The first integral can be derived exactly from Eq. (14), and the second integral is produced by the finite element solver. Plotting the error energy norm given by Eq.(19) versus the number of degrees of freedom or mesh vertices indicates the accuracy of the solver. The results are shown in Figure 15. The asymptotic convergence rates approach the linear rate as predicted by Eq. (20). It is expected the results will approach the quadratic rate when quadratic finite element analysis is implemented in the Phase II program.

This task demonstrated that the solver accuracy and convergence rate match the theoretical solution and rate, respectively.

### *Task 3.Improve the accuracy and smoothness of the power density fields at the terminal surfaces*

BOA generates the power density fields, interpolating the particle energies to the mesh vertices on the terminal surface, as follows,

$$E_n = N_n(\mathbf{x})E(\mathbf{x}) \tag{21}$$

where $E_n$ is the particle energy interpolated to the vertex $n$, $\mathbf{x}$ the particle position, $E$ particle energy at $\mathbf{x}$, and $N_n$ the interpolation, shape function. After all particle energies are accumulated to the vertex $n$, its power density can be calculated by the following formula

$$W_n = \frac{E_n}{\sum_{m=1}^{M} \int_{\Omega_m} N_n d\Omega} \tag{22}$$

where $M$ is the number of finite elements adjacent to the same vertex $n$, and $\Omega_m$ is the volume of the $m^{th}$ element sharing this same vertex. Power density fields displayed in Figure 4 and Figure 8b are first generated by linear Lagrange shape functions then smoothed by the $L^2$ projection to the quadratic Lagrange space. The heat transfer solver in BOA then uses this quadratic power density field as the heat flux boundary condition. It will use the quadratic Lagrange shape function to interpolate the power density field when computing the element integrals in the matrix assembly phase. The *SPR* scheme described earlier to smooth the gradient field is only applicable to linear space. It cannot be used to smooth the power density field by increasing the field interpolation order from linear to quadratic. The $L^2$ projection, which is the multidimensional version of the 1D least squares curve fit, is needed for higher order spaces. There are two ways to implement the $L^2$ projection, *locally* or *globally*. In the local scheme, the field in each element is projected from linear to quadratic integrally. For each mesh vertex, a patch of elements adjacent to it (the same as the SPR scheme) is then formed. The element projected fields in the patch are now averaged using another $L^2$ projection, but from quadratic to quadratic space to obtain the global field at each vertex. In the global scheme, the whole linear field is simply projected to the quadratic space. Due to the limited scope of the Phase I program, only the global $L^2$ projection of the power density field was implemented.

To investigate the effectiveness of the global $L^2$ projection of the power density field on improving the temperature fidelity, let us revisit the electron gun in Figure 1. The linear power density on the anode cap is shown in Figure 16a and the quadratically projected power density field in Figure 16b. The quadratic field shows a higher resolution of a narrower concentration of field at the center.

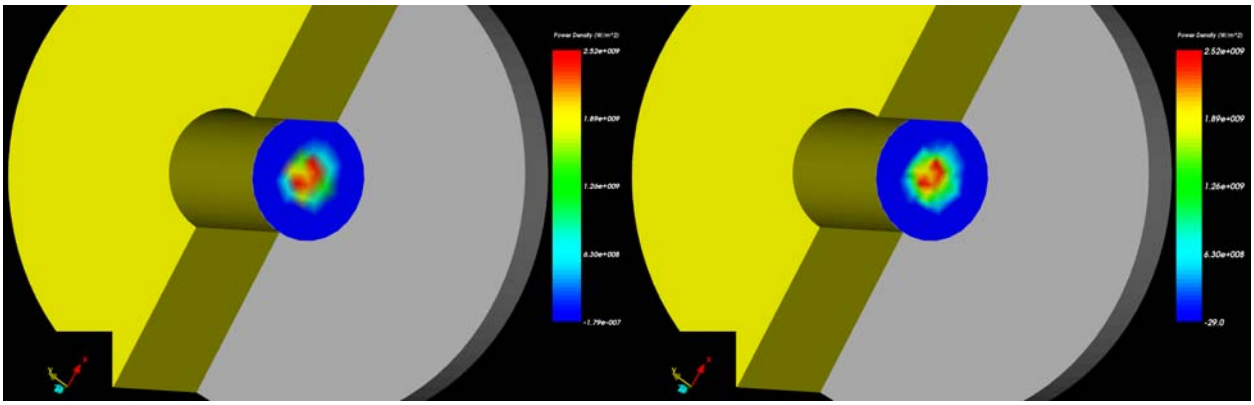


**Figure 16** Power density field on the anode cap **(a)** linear field **(b)** quadratically projected field

Figure 17a shows the temperature on the anode cap generated by the linear power density field, and Figure 17b shows the quadratic power density field. There are few noticeable differences between the two profiles. The line plot of the temperature on the anode cap along the y axis confirms this observation, as shown in Figure 18.

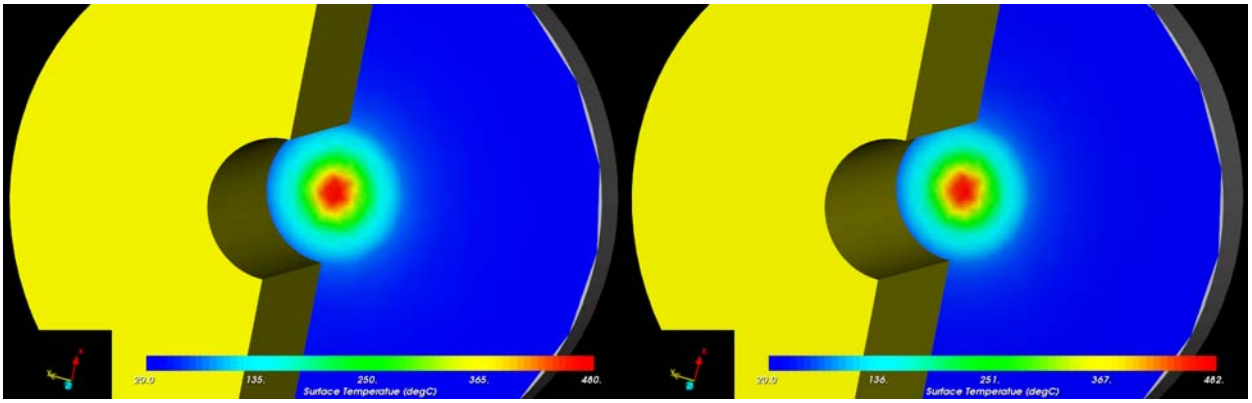


**Figure 17** Temperature profile on anode cap **(a)** from linear **(b)** quadratic power density field

Due to the ballistic nature of electrons and the linear interpolation from the particle positions and energies to the mesh, the power density field is neither smooth nor uniform. Prior to the Phase I program, it was anticipated that improving the field fidelity by increasing the order of interpolation for the power density field would improve the temperature resolution. However, the above results appear to indicate that a higher order power density field does not translate to major differences in the heat transfer solution. It is conceivable that the global $L^2$ projection generates excessive damping and overlooks the local variations of the field. In the Phase II program, the local $L^2$ projection will be implemented to revisit using higher order power density for heat transfer analysis. Although implementation of the global $L^2$ projection does not improve the heat transfer solution, the quadratic shape function to interpolate the higher order power density field is complete and ready for the higher order solver in the Phase II.

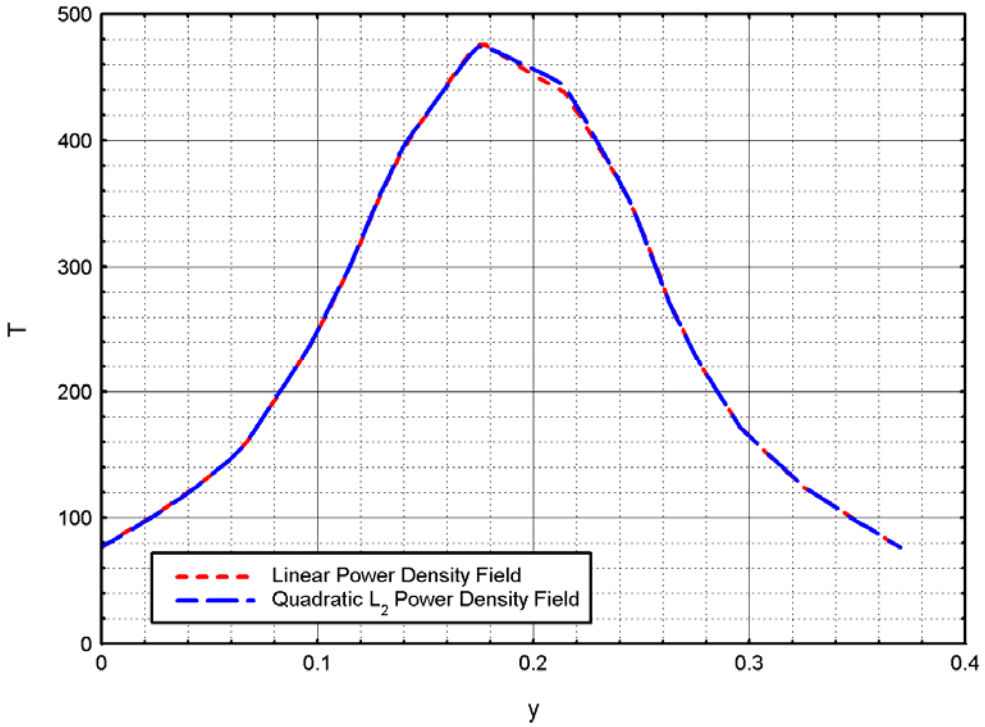


**Figure 18** Temperature on the anode cap along the y axis. Practically identical using either linear or quadratic power density field.

## Task 4. Design GUI windows for heat transfer problems

The heat transfer in BOA is fully functional in terms of solution accuracy, stability and robustness. The Phase I program also integrated a GUI for entering geometry (see Figure 1), selecting analysis type, slicing and viewing the model in different ways, and displaying different axes, particle colors, etc. The GUI also allows selection of materials from a built-in database that includes the appropriate material properties for the analysis selected. Figure 19 displays the electrostatics and heat transfer screens showing the same part names and materials, but with different boundary conditions appropriate to the analysis type. In the heat transfer screen, the user specifies the heat source or temperature in a solid part. He can also prescribe the temperature or heat flux or convection cooling on a surface.

The Phase I program extended the fine grain meshing control in BOA to create the mesh for heat transfer analysis. Particular model entities, parts, or surfaces can be selected to specify their mesh sizes as shown in Figure 20. Free mesh regions or surface constrained regions can be specified either cylindrical or rectangular prism as shown in Figure 21. Since each analysis type maintains its own mesh, it also maintains its own meshing parameters, allowing very flexible control to invoke finer meshes in particular entities in one analysis type but coarser meshes in another type. These local refinement meshes can be refined but not coarsened during the adaptivity process.

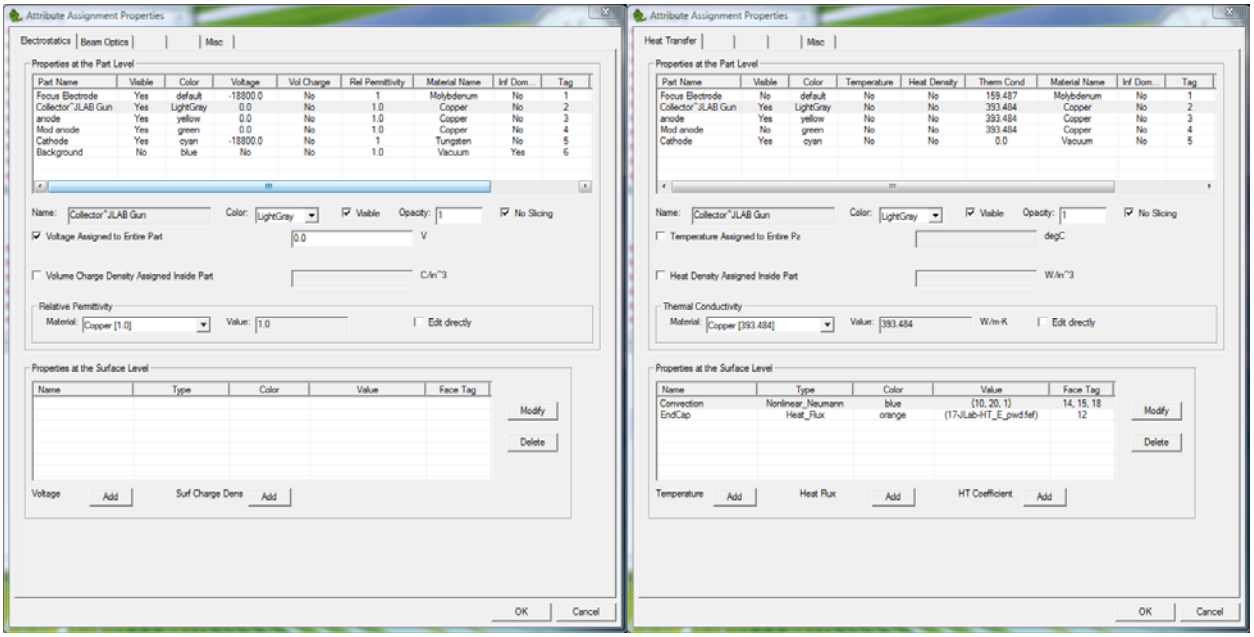

**Figure 19.** BOA Attribute Assignment Windows for Electrostatics and Heat Transfer. Materials can be selected from a list of built-in or user's defined materials.

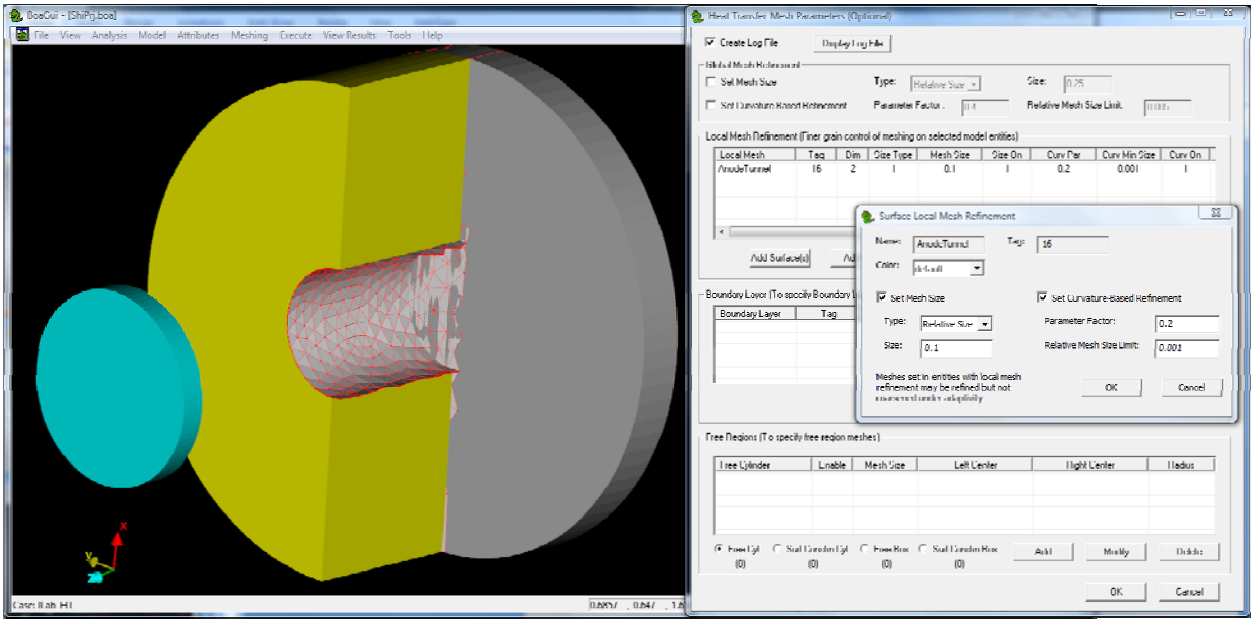

**Figure 20** GUI screen for heat transfer to specify local meshing on model entities including free mesh regions

Although CCR originally planned only to design GUI panels to control the field processing of heat transfer solutions in Phase I, we found that to be able to diagnose and verify the code, it was much more efficient to have a complete post-processor. We decided to complete the GUI driven post-processor for processing the heat transfer solution fields in Phase I. As displayed in Figure 5, Figure 6, Figure 8, Figure 12, Figure 16, Figure 17 and Figure 22, the heat transfer fields can be displayed along a line, on a surface, or in a region. The post-processor window is shown in Figure 22.

This task completed the heat transfer post-processor to display fields at a point, along a line, on a surface and in a part. Meshes producing the solution fields, either initial or adapted, can also be displayed.

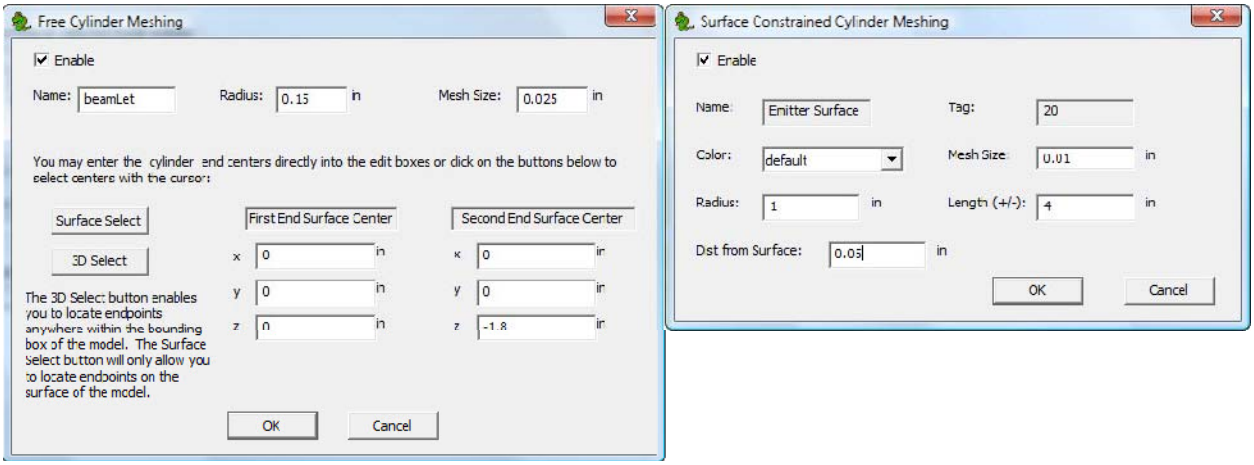


**Figure 21 (a)** Free cylinder mesh, both end face centers must be specified **(b)** Surface constrained cylinder mesh, length is required

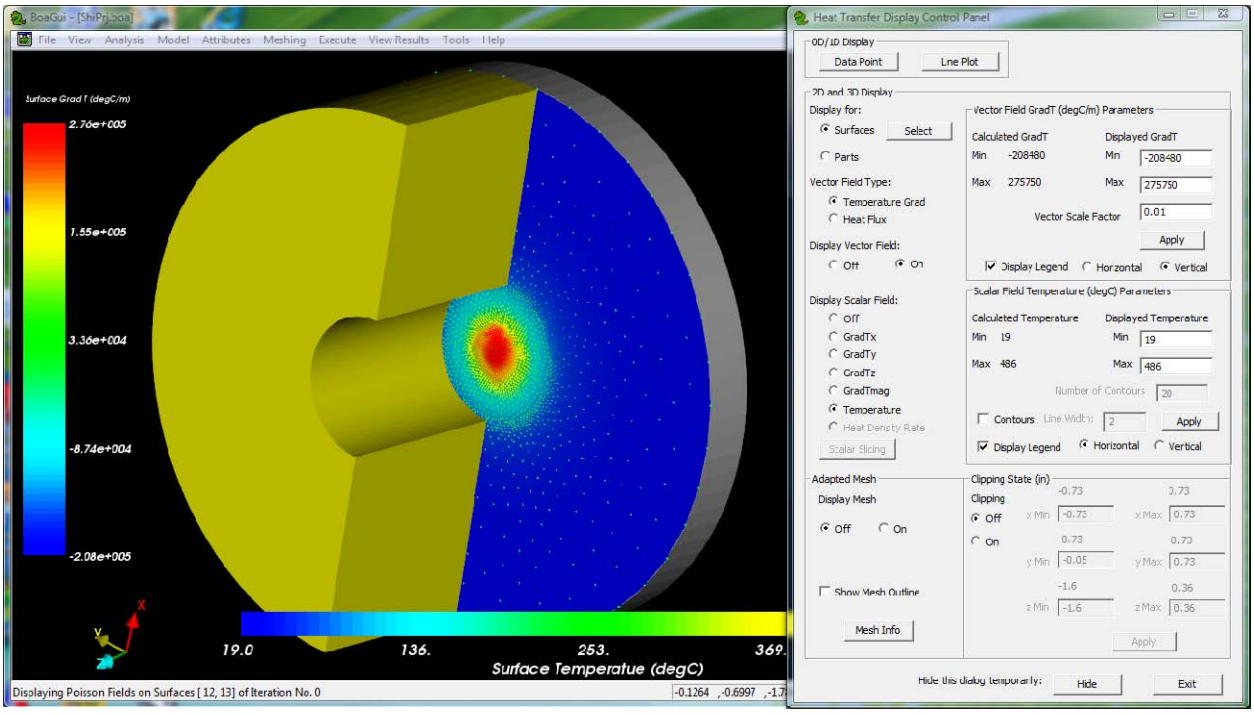


**Figure 22** Heat transfer post-processor panel to display fields on a point, line, surface and part

## Summary

The Phase I program originally only planned to demonstrate the stability, accuracy, and convergence of the heat transfer solver, examine the integration issues with sharing models and meshes, and design the post-processor panel to display solution fields. The Phase I program not only accomplished these tasks but also completed the heat transfer integration with beam optics analysis in BOA. Beam Optics Analyzer is now fully capable of performing thermal analysis

using the beam generated power density with convection cooling. Using the same CAD model, BOA can seamlessly maintain different meshes, material properties and boundary conditions for each analysis type.

There are still a number of tasks remaining to complete the development. The heat transfer solver currently assumes isotropic and linear materials. Anisotropic materials such, as pyrolytic graphite, cannot be modeled correctly. Devices operated at high temperature causing thermal conductivity variations require a nonlinear solver. High temperature devices also require radiation heat transfer between surfaces, which is a very highly nonlinear process. The heat transfer coefficients, which are functions of flow rate, temperature, coolant properties and geometry, can often be empirically calculated. Users must currently provide their own calculated values. It would be much more convenient to provide a heat transfer coefficient calculator. One would only need to select a cross section from standard shapes to specify its dimension, flow rate, coolant temperature and type. The calculator would determine the heat transfer coefficient and automatically update the database if convection cooling was prescribed to a model face. This approach could also be extended the current collector optimization by including not only the beam optics performance, but also the cooling requirements.

Since BOA includes time dependent PIC capability and can use time-dependent, spent beam data from a large signal code, the beam generated power density field could also be time-dependent. A transient heat transfer solver would then be required to accurately obtain the device thermal characteristics. More accuracy and higher field fidelity are highly desirable, and currently the Phase I solver includes only linear elements. Quadratic finite elements would improve the solution accuracy. Quadratic interpolation, including adaptivity, would not only improve solution fidelity but also maintain a coarser mesh than the linear version.

Once temperature profiles for a device are determined, designers are often concerned with thermally induced stresses. In addition, particle beam vacuum devices under thermal stresses are subjected to induced and ambient pressures. It would be highly desirable to have a single design tool integrating beam optics, heat transfer, and stress analysis.

## References


1. CCR Inc., *Development of a Finite Element, Adaptive Mesh Charged Particle Code*, U.S. Dept. of Energy Grant No. DE-FG-03-00ER82966, Sept. 2000 to June 2003.
2. T. Bui et. al., *Beam Optics Analysis – A 3D Finite Element Charged Particle Code with Adaptive Meshing*, Paper 9.3, IVEC, Monterey, CA, USA, 2002.
3. T. Bui et. al., *Initial Operation of Beam Optics Analysis, a 3D, Charged Particle Code with Adaptive Meshing, Paper 2A02*, ICOPS, Banff, Alberta, Canada, 2002.
4. T. Bui et. al., *Code Development of a 3D Finite Element Particle-In-Cell Code with Adaptive Meshing*, IVEC, Noordwijk, The Netherlands, 2005.
5. T. Bui et. al., *Code Development of a 3D Finite Element Particle-In-Cell Code with Adaptive Meshing*, ICOPS, Monterey, CA, USA, 2005.
6. C.T. Kelley, *Iterative Methods for Optimization*, SIAM, Philadelphia, 1999.
7. J. David, *Optimal Control, Estimation, and Shape Design: Analysis and Application*, 2007. PhD Thesis, North Carolina State University.

8. T. Bui et. al., *An Optimizer for Beam Optics Analyze*r, IVEC, Rome, Italy, 2009.
9. T. Bui et. al., *An Optimizer for Beam Optics Analyzer*, ICOP-SOFE. San Diego, CA, USA, 2009.
10. T. Hughes, *The Finite Element Method*, Prentice-Hall (Englewood Cliffs, NJ), 1987.
11. T. Bui, L. Ives, M. Read, *Heat Transfer Integration with Beam Optics Analyzer*, IVEC, Bangalore, India, 2011.
12. T. Bui, M. Read, L. Ives, *Temporal Particle-In-Cell Analysis in Beam Optics Analyzer*, IVEC, Bangalore, India, 2011.
13. B. Szabo and I. Babuska, *Finite Element Analysis*, John Wiley & Sons (New York), 1991.
14. O.C. Zienkiewicz and J.Z. Zhu, *The superconvergent patch recovery and a posteriori error estimates. Part 1: The recovery technique*. International Journal of Numerical Methods in Engineering, 33:1331-1364, 1992.
15. O.C. Zienkiewicz and J.Z. Zhu, *The superconvergent patch recovery and a posteriori error estimates. Part 2: The recovery technique*. International Journal of Numerical Methods in Engineering, 33:1365-1382, 1992.
16. N. Yan and A. Zhou, *Gradient recovery type of a posteriori error estimates for finite element approximation on irregular meshes*, Computer Methods in Applied Mechanics and Engineering, Vol. 190, 2001.
17. M. Ainsworth and J.T. Oden, *A Posteriori Error Estimation in Finite Element Analysis*, John Wiley & Sons (New York), 2000.
18. L.B. Wahlbin, *Superconvergence in Galerkin Finite Element Methods*, Vol. 1605 of Lecture Notes in Mathematics. Springer-Verlag, 1995.] B.N, Lewis, H.T. Tran, R.L. Ives, M. Read, *Design of and Electron Gun Using Computer Optimization*, IEEE Trans. on Plasma Sci. Vol. 32, No. 3, 1242-1250, June 2004.
19. R. Lawrence Ives, A. Attarian, T. Bui, M. Read, J. David, H. Tran, W. Tallis, S. Davis, S.E. Gadson, N. Blach, D. Brown, E. Kiley, *Computational Design of Asymmetric Electron Beam Devices*, IEEE Trans. on Electron Devices, Vol. 56, No. 5, May 2009.
20. C.T. Kelley, *Solving Nonlinear Equations with Newton's method*, SIAM (Philadelphia), 2003.
21. T. Bui, *Beam Optics Analyzer, A Particle-In-Cell Code, Phase II Final Report for DOE*, CCR, November 2007.
22. R. Seigel, J.R. Howell, *Thermal Radiation Heat Transfer* (2rd ed.), Hemisphere (New York), 1981.
23. W.M. Kay, M.E. Crawford, *Convective Heat and Mass Transfer* (2rd ed.), MacGraw-Hill (New York), 1980.
24. J.E. Marsden, T Hughes, *Mathematical Foundation of Elasticity*, Prentice-Hall (Englewood Cliffs), 1983.